International Journal of Solids and Structures 50 (2013) 1523–1537

Contents lists available at SciVerse ScienceDirect

International Journal of Solids and Structures

journal homepage: www.elsevier.com/locate/ijsolstr

Three-dimensional recovery of stress intensity factors and energy release rates from surface full-field displacements

Stéphane Andrieux [a], Thouraya Nouri Baranger [b,*]

[a] Laboratoire de mécanique des structures industrielles durables, CNRS: UMR 2832, EDF Recherche & Développement 1, avenue du Général de Gaulle, 92141 Clamart Cedex, France
[b] Université de Lyon, CNRS, Université Lyon1, Laboratoire de mécanique des contacts et des structures, UMR 5259, 18-20 rue des sciences, F69621 Villeurbanne cedex, France

ARTICLE INFO

Article history:
Received 1 October 2012
Received in revised form 15 December 2012
Available online 23 January 2013

Keywords:
Cauchy problem
Elasticity
Full-field displacements
Linear fracture mechanics
Stress intensity factors
Identification
Data completion

ABSTRACT

The identification of stress intensity factors (SIFs) from full-field displacement measurements by the optic method is accelerating rapidly following the development of precise digital cameras and image correlation algorithms. Nevertheless, as only surface displacements are available, most of the identification methods used up to now have been restricted to problems that are invariant with respect to the normal direction of the free surface and must rely on the plane elasticity hypothesis. The problem of SIFs identification is tackled here in a full three-dimensional framework by first deriving a data completion method in elasticity to determine the elastic displacement field inside the solid on the basis of surface displacements. The method solves the Cauchy problem for the Lamé operator after which usual numerical methods for computing SIFs and energy release rates can be used. Numerical applications in three-dimensional elasticity are described first for a cracked specimen subjected to 3D loadings and, secondly, for a heterogeneous specimen in a quasi-plane situation.

1. Introduction

The development of digital image correlation (DIC) techniques has led to using the full-field displacement on a plane surface provided by these techniques for determining the parameters of linear fracture mechanics. The use of full-field displacement has received considerable attention since the pioneering work of McNeill et al. (1983, 1987) and then those of (Hild and Roux, 2006; Ju et al., 2006; Yoneyama et al., 2007; Yates et al., 2010). The problems tackled are quasi-plane problems Fig. 1, which are situations where the geometry and the applied loads are invariant in the direction parallel to the (rectilinear) crack front. The analysis is generally conducted within the plane stress framework by using correlation techniques that try to fit the actual measured in-plane displacement fields with analytical or numerical fields, or compute independent paths or interaction integrals.

Extending the application of fracture mechanics parameter identification from DIC displacement field to truly 3D situations has attracted increasing attention for three mains reasons. The first is that it can deal with more complicated experiments or in-service structures that have non-directionally invariant geometries and are subjected to truly 3D loads. The second is that even for quasi-plane situations it is known that boundary layer effects exist for moderately thin structures, especially for bi-materials (Rosakis and Ravi-Chandar, 1986; Sinha et al., 1997; Li et al., 2000). In this case, the estimated fracture mechanics parameters can differ significantly from those averaged through-the-thickness if surface fields and the assumption of plane stress are used. The last reason is that from the theoretical standpoint, Leblond (2003), demonstrated numerically by Noda and Kagita (2004), the singularity of surface fields is not the same as for the bulk fields and is therefore different from the $r^{1/2}$ classical form for the displacement field. It can therefore be expected that fitting the displacement fields with the *"wrong"* asymptotic form can lead to a supplementary error on SIFs (Stress Intensity Factors) and fracture parameters.

To achieve our goal, we propose in this paper to first numerically extend the tangential surface displacement field, provided on a part of the external boundary, within the entire solid, and then use standard numerical procedures to compute the fracture mechanics parameters along the crack front such as SIFs or elastic energy release rates.

The paper first recalls the basic notions and computational methods in linear fracture mechanics, pointing out several *"boundary layer or surface effects"* identified in the literature from both computational and experimental viewpoints. Next, a quick review is given of the numerical procedures used for SIFs identification from full field (in-plane) displacements. The procedure used to extend the surface displacement field and based on the solution of a Cauchy problem by energy gap functional minimization, is then described. Finally, two 3D examples illustrating the method are

* Corresponding author.
E-mail addresses: Stephane.Andrieux@edf.fr (S. Andrieux), Thouraya.Baranger@univ-lyon1.fr (T.N. Baranger).

0020-7683/$ - see front matter © 2013 Elsevier Ltd. All rights reserved.
http://dx.doi.org/10.1016/j.ijsolstr.2013.01.002

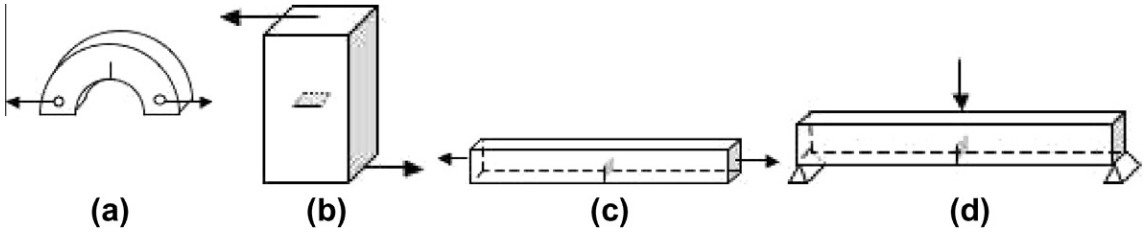

Fig. 1. Examples of quasi-plane problems.

presented: the first is a 3D loading on a simple homogeneous cracked specimen; the second is a quasi-plane problem but for a bi-material CT specimen.

2. Stress intensity factors and energy release rates in linear fracture mechanics

2.1. Preliminaries

Let us consider the general three-dimensional problem for a cracked solid $\Omega \setminus \Gamma$, where Γ is the stress-free crack surface. We denote the displacement field by $\mathbf{u}, \sigma$ is the Cauchy stress tensor and ε is the linearized strain tensor.

2.1.1. Cracks in two dimensions

If the solid and the crack geometry are invariant in the z direction, and if the loading has the same property, then the problem can be viewed as a plane problem. The singular *asymptotic* stress-field solution of Williams (1957), based on the Airy function in polar coordinates for plane elasticity is written as:

$$\sigma_{rr} = \frac{K_I}{4\sqrt{2\pi r}}\left[5\cos\frac{\theta}{2} - \cos\frac{3\theta}{2}\right] + \frac{K_{II}}{4\sqrt{2\pi r}}\left[-5\sin\frac{\theta}{2} + 3\sin\frac{3\theta}{2}\right] \quad (1)$$

$$\sigma_{\theta\theta} = \frac{K_I}{4\sqrt{2\pi r}}\left[3\cos\frac{\theta}{2} + \cos\frac{3\theta}{2}\right] + \frac{K_{II}}{4\sqrt{2\pi r}}\left[-3\sin\frac{\theta}{2} - 3\sin\frac{3\theta}{2}\right] \quad (2)$$

$$\sigma_{r\theta} = \frac{K_I}{4\sqrt{2\pi r}}\left[\sin\frac{\theta}{2} + \sin\frac{3\theta}{2}\right] + \frac{K_{II}}{4\sqrt{2\pi r}}\left[\cos\frac{\theta}{2} + 3\cos\frac{3\theta}{2}\right] \quad (3)$$

The displacement field $\mathbf{u}$ is obtained by integrating the strain deduced via the elastic constitutive equation for isotropic solids, where E is the Young modulus and ν is the Poisson ratio:

$$\mathbf{u} = K_I\mathbf{u}^I + K_{II}\mathbf{u}^{II} \quad (4)$$

$$\mathbf{u}^I = \begin{bmatrix} u_r^I \\ u_\theta^I \end{bmatrix} = \sqrt{\frac{r}{2\pi}}\frac{(1+\nu)}{E}\begin{bmatrix} (\frac{5}{2} - 4\bar{\nu})\cos\frac{\theta}{2} - \frac{1}{2}\cos\frac{3\theta}{2} \\ -(\frac{7}{2} - 4\bar{\nu})\sin\frac{\theta}{2} + \frac{1}{2}\sin\frac{3\theta}{2} \end{bmatrix} \quad (5)$$

$$\mathbf{u}^{II} = \begin{bmatrix} u_r^{II} \\ u_\theta^{II} \end{bmatrix} = \sqrt{\frac{r}{2\pi}}\frac{(1+\nu)}{E}\begin{bmatrix} (-3 + 4\bar{\nu})\sin\frac{\theta}{2} + \sin\frac{3\theta}{2} \\ -(\frac{7}{2} - 4\bar{\nu})\cos\frac{\theta}{2} + \frac{3}{2}\cos\frac{3\theta}{2} \end{bmatrix} \quad (6)$$

where $\bar{\nu} = \nu$ for plane strain and $\bar{\nu} = \nu/(1+\nu)$ for plane stress. The solution is completed, under the plane strain condition by the expression of stress σ_{zz} normal to the plane:

$$\sigma_{zz} = \nu(\sigma_{rr} + \sigma_{\theta\theta}) \quad (7)$$

Under plane stress conditions the solution is completed by the expression of strain component ε_{zz} normal to the plane:

$$\varepsilon_{zz} = -\frac{\nu}{E}(\sigma_{rr} + \sigma_{\theta\theta}) = -\frac{\nu}{1-\nu}(\varepsilon_{rr} + \varepsilon_{\theta\theta}) \quad (8)$$

Consider a plate $\frac{-h}{2} \leqslant z \leqslant \frac{h}{2}$, the plane stress elasticity equations are only an approximation of the full 3D equations. Here it is straightforward to observe that the calculus of the normal displacement field and the other components of the strain tensor, i.e.:

$$u_z(r,\theta,z) = z\varepsilon_{zz}(r,\theta) + F(r,\theta), \quad 2\varepsilon_{rz} = \frac{\partial u_z}{\partial r}, \quad 2\varepsilon_{\theta z} = \frac{1}{r}\frac{\partial u_z}{\partial \theta} \quad (9)$$

lead to non-bounded displacements in the vicinity of the crack tip, and non zero transverse shear stresses, except on midplane $z = 0$.

Another standpoint in linear fracture mechanics theory is the energetic approach where the severity of the loading on the solid is measured by Griffith's energy release rate G, which is simply defined for a linear crack in two dimensions by the opposite of the derivative with respect to crack length l of the equilibrium values of the potential energy of the solid:

$$\begin{cases} G = -\frac{\partial}{\partial l}W_{eq}^{pot}(l,P) & (10a) \\ W_{eq}^{pot}(l,P) = \min\limits_{\mathbf{u}\in KA(l)} \int_{\Omega(l)} \varphi(\varepsilon(\mathbf{u}))d\Omega + W^{ext}(P,\mathbf{u}) & (10b) \end{cases}$$

where P stands for the loading applied to the solid, W_{eq}^{pot} is its potential energy at equilibrium, ϕ is the elastic strain energy density and KA the space of kinematically admissible displacement fields (which depend on crack length). The link with the SIFs is given in this two-dimensions setting by the following Irwin's formula (Irwin, 1957; Bui, 1978; Leblond, 2003):

$$G = \frac{1}{\bar{E}}\left(K_I^2 + K_{II}^2\right) \quad (11)$$

with $\bar{E} = E$ for the plane strain conditions and $\bar{E} = E/(1-\nu^2)$ for the plane stress conditions.

2.1.2. Three-dimensional Cracks

For 3D cracks, excepting points on the external surface, the general asymptotic elastostatic solution is described as a combination of the three mode fields in each plane containing the normal vector $\mathbf{N}$ to the tangent plane of the crack surface and the normal vector $\mathbf{n}$ to the crack front γ, parametrized by the curvilinear abscissa s as shown in Fig. 2a and b (see Bui, 1978, 2006; Leblond, 2003).

The mode I and II fields are the strain modes acting in the plane $(\mathbf{N},\mathbf{n})$, with $K_I(s)$ and $K_{II}(s)$ being functions of abscissa s, whereas the mode III field is the anti-plane field, such that:

$$\sigma_{rs} = \frac{K_{III}(s)}{\sqrt{2\pi r}}\sin\frac{\theta}{2} \quad (12)$$

$$\sigma_{\theta s} = \frac{K_{III}(s)}{\sqrt{2\pi r}}\cos\frac{\theta}{2} \quad (13)$$

$$u_s = K_{III}(s)\frac{4(1+\nu)}{E}\sqrt{\frac{r}{2\pi}}\sin\frac{\theta}{2} \quad (14)$$

For 3D cracks, the virtual extension of the crack is no longer a scalar and is described by the positive scalar normal celerity function $c(s)$ defined on the crack front γ. In this extension, each geometrical point $M(s)$ on the crack front is translated in direction $\mathbf{n}(s)$ by an amount of $c(s)$ as shown on Fig. 2b. So that, for example, the variation of the crack area is:

$$\delta|\Sigma| = \int_\gamma c(s)ds \quad (15)$$

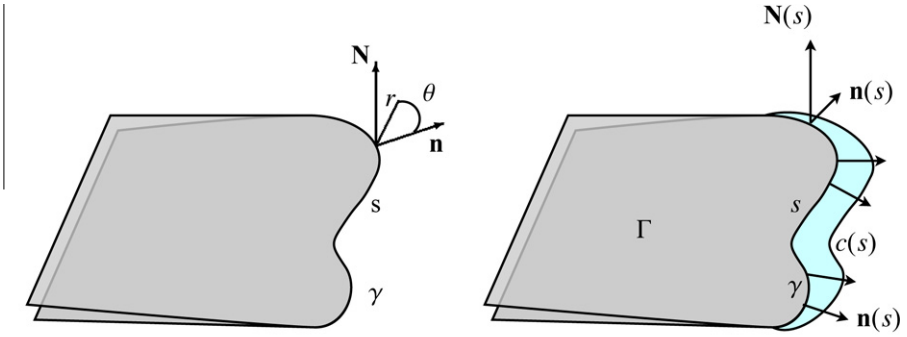

(a) Geometry of the three-dimensional crack. (b) Normal celerity and extension of a 3D crack.

Fig. 2. Crack front and some definitions.

The energy release rate $G(c)$ in the extension defined by $c(s)$ is therefore the directional derivative:

$$G(c) = -\lim_{h\to 0}\frac{1}{h}\left[W_{eq}^{pot}(\Sigma + \delta\Sigma(hc), P) - W_{eq}^{pot}(\Sigma, P)\right] \tag{16}$$

For sufficiently regular cracks and loading, the energy release rate $G(c)$ can be represented by a linear form acting on the normal celerity, where $g(s)$ is the local energy release rate defined as follows:

$$G(c) = \int_{\gamma} g(s)\, c(s) ds \tag{17}$$

and the Irwin formula again provides a link with the local SIFs:

$$g(s) = \frac{1}{E}(K_I(s)^2 + K_{II}(s)^2) + \left(\frac{1+\nu}{E}\right)K_{III}(s)^2 \tag{18}$$

2.2. Invariant volume and surface integrals for the computation of energy release rates and SIFs

Various methods have been proposed to compute the SIFs and the energy release rate on the basis of knowledge of the displacement field throughout the solid, obtained by the numerical resolution of the direct elastostatic problem. An initial family of methods is directly related to the asymptotic behavior of these fields around the crack tip:

$$\begin{cases} K_I = \lim_{r\to 0} \frac{8E}{(1-\bar{\nu})(1+\nu)}[\![u_1(r)]\!]\sqrt{\frac{2\pi}{r}} & \text{(19a)} \\ K_{II} = \lim_{r\to 0} \frac{8E}{(1-\bar{\nu})(1+\nu)}[\![u_2(r)]\!]\sqrt{\frac{2\pi}{r}} & \text{(19b)} \\ K_{III} = \lim_{r\to 0} \frac{8E}{(1+\nu)}[\![u_3(r)]\!]\sqrt{\frac{2\pi}{r}} & \text{(19c)} \end{cases}$$

where $\bar{\nu} = \nu$ stands for plane strain conditions and $\bar{\nu} = \nu/(1+\nu)$ for plane stress conditions. And a displacement correlation method is necessary in order to extract the SIFs. Therefore a least-squares method can be used. In plane $(\mathbf{n}(s), \mathbf{N}(s))$, once a segment $[0, r_m]$ has been selected along the crack lips, where $r = 0$ corresponds to the crack front, the SIFs can be computed by the following formula, (see Galenne et al., 2005):

$$K_i(s) = \sqrt{\frac{\pi}{8}}\frac{E}{(1-\varepsilon_i\nu)(1+\nu)r_m^2}\int_0^{r_m}[u_i(r,\pi,s) - u_i(r,-\pi,s)]\sqrt{r}dr,$$
$$i = I, II, III, \quad \varepsilon_I = \varepsilon_{II} = 1, \quad \varepsilon_{III} = 0 \tag{20}$$

Corresponding procedures for SIFs evaluation by using full-field displacements have been designed in the same way, but as will be described in Section 4, higher order terms of the solution to the Williams' series must also be used. Another family of methods is based on the computation of invariant integrals on surfaces or volumes surrounding the crack tip. They are first intended to compute the global elastic energy release rate for a uniform normalized normal celerity along the crack front and are based on Rice's path-independent integral J (Rice, 1968):

$$G = J \equiv \int_{\mathcal{C}}[\varphi\mathbf{n}\cdot\vartheta - \sigma_{\mathbf{n}i}u_{i,\mathbf{n}}]\, d\mathcal{C} \tag{21}$$

where $\mathcal{C}$ is any closed surface surrounding the crack front and ϑ the outward unit normal at $\mathcal{C}$. The virtual extension method is used to compute the local energy release rate $g(s)$ and also to insure better robustness and stability of the results for finite element computations. In (Destuynder and Jaoua, 1981; Destuynder et al., 1983) a virtual extension C^1 vector field $\theta(x)$ is introduced with the property in each plane $(\mathbf{n}(s), \mathbf{N}(s))$ to be normal to the crack front γ at s, such as:

$$\begin{cases} \theta(x_{\mathbf{n}}, x_{\mathbf{N}}, s) = c(s)\mathbf{n}(s) & \text{for } (x_{\mathbf{n}}, x_{\mathbf{N}}) \in \Omega_1 \\ \theta(x_{\mathbf{n}}, x_{\mathbf{N}}, s) = 0 & \text{for } (x_{\mathbf{n}}, x_{\mathbf{N}}) \in \Omega_2 \\ \theta \text{ regular} & \text{for } (x_{\mathbf{n}}, x_{\mathbf{N}}) \in \Omega_{12} \end{cases} \tag{22}$$

χ_1 and χ_2 are two regular curves so that $C_i = \chi_i \times [0,1]$ for $i = 1, 2$ are regular surfaces enclosing the crack front as shown in Fig. 3, Ω_1 is the interior domain enclosed by curve χ_1 in the $(\mathbf{n}(s), \mathbf{N}(s))$ plane, Ω_2 is the exterior domain of curve χ_2 and Ω_{12} is the domain delimited by the two curves, χ_1 and χ_2.

The energy release rate can be expressed by the following domain invariant integral:

$$\begin{aligned} G(c) &= -\int_{\Omega_{12}}[\varphi div\theta - \sigma\cdot\nabla u\cdot\nabla\theta]\, d\Omega \\ &= -\int_{\Omega_{12}}[\varphi\,\theta_{l,l} - \sigma_{ij}u_{i,l}\theta_{l,j}]\, d\Omega \end{aligned} \tag{23}$$

The determination of the local energy release rate $g(s)$ requires solving Eq. (17). Different discretizations along the crack front can be used for the normal celerity functions $c(s)$ and the local release

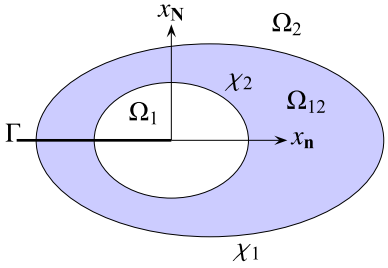

Fig. 3. Definition of sub-domains for the virtual crack extension method.

rate $g(s)$, Galenne et al. (2005). This approach is known as G-Theta method.

An elegant computation method for the SIFs can then be deduced in two dimensions by noting that the energy release rate G is a quadratic form acting on displacement fields: $G = G(\mathbf{u})$. Then, by considering the associated bilinear form $B_G(\mathbf{u},\mathbf{v})$, obtained by the polarization equation:

$$B_G(\mathbf{u},\mathbf{v}) = \frac{1}{4}(G(\mathbf{u}+\mathbf{v}) - G(\mathbf{u}-\mathbf{v})) \tag{24}$$

and by using Irwin formula, it is clear that the bilinear form can be expressed with the SIFs corresponding to fields $\mathbf{u}$ and $\mathbf{v}$:

$$\begin{aligned} B_G(\mathbf{u},\mathbf{v}) &= \frac{1}{4}(G(\mathbf{u}+\mathbf{v}) - G(\mathbf{u}-\mathbf{v})) \\ &= \frac{1}{4\overline{E}}\left(K_I(\mathbf{u}+\mathbf{v})^2 + K_{II}(\mathbf{u}+\mathbf{v})^2 - K_I(\mathbf{u}-\mathbf{v})^2 - K_{II}(\mathbf{u}-\mathbf{v})^2\right) \\ &= \frac{1}{\overline{E}}(K_I(\mathbf{u})K_I(\mathbf{v}) + K_{II}(\mathbf{u})K_{II}(\mathbf{v})) \end{aligned} \tag{25}$$

Then, by selecting the singular fields $\mathbf{u}^I$ and $\mathbf{u}^{II}$ for the $\mathbf{v}$ fields, we obtain the formula for the separate computation of the SIFs associated with $\mathbf{u}$:

$$K_I(\mathbf{u}) = \overline{E}B_G(\mathbf{u},\mathbf{u}^I), \quad K_{II}(\mathbf{u}) = \overline{E}B_G(\mathbf{u},\mathbf{u}^{II}) \tag{26}$$

The domain-integral expression of B_G is known as the interaction integral (similar definition and results can be derived from the path-independent integral J). The method is also referred to as the auxiliary fields method in (Bui, 1983).

3. Three dimensional effects in linear fracture mechanics

Parsons and Hall (1989), performed a numerical study of the simple problem of an edge crack in a plate under tension with thickness h. The results showed that the in-plane stress, σ_{ij} with $(i,j) = (r,\theta)$, were nearly constant through the thickness with the normal stresses falling by approximately 25% at the free surfaces. The out-of-plane stress component σ_{33} varied considerably through the thickness. The results also showed that at the center of the plate, very close to the crack tip, the stress field was a plane strain field, as expected. Further away from the crack, $r \approx 0.33h$ the field was a plane stress. Very close to the crack tip, the plane strain predominated except in a boundary layer near the free surfaces.

Rosakis and Ravi-Chandar (1986), showed that the size of the three dimensional effect on the surface fields extended approximately to a radius equal to half the thickness h of the solid.

Sinha et al. (1997), investigated mixed mode for interfacial cracks in a PMMA/ Al specimen subject to three point bending by experimental interferometric means coupled with finite element analysis. For dominant tensile stress conditions, plane stress conditions were not established along the bond line, even far away from the crack tip. At other polar directions (65° to 135°) plane stress conditions were encountered at distances greater than $0.3h$. However, there was a significant reduction of these strong 3D effects for dominant shear stress conditions.

For notches, Li et al. (1985), extensively studied the effect of finite thickness of the plate. For small quarter-elliptical corner cracks in elastic plates subjected to tension, Zhang and Guo (2007), used finite element analysis to demonstrate that strong 3D effects exist within a radial distance of the crack tip ranging from $4.6a$ to $0.7a$, a and c being respectively the minor and major semi axes, for an aspect ratio c/a ranging from 0.2 to 1.

For semi-elliptical surface cracks, it is known that the asymptotic form or the stress singularity of the elastic solution at the point where the crack front intersects with the free surface is different from the $r^{1/2}$ ordinary form. The actual exponent is Poisson ratio and Mode dependant. It varies in the range 0.332–0.5 for the Mode I solution, and in the range 0.5–0.646 for the mode II and III solutions, for Poisson ratios varying from 0 to 0.5. Noda and Kagita (2004) reviewed existing solutions and proposed a method based on the body force method with a highly singular fundamental solution for accurately computing stress intensity factors along the crack front of semi-elliptic and rectangular cracks.

4. SIFs determination from digital image correlation

4.1. SIFs determination methods with digital image correlation

Let us assume that a surface displacement field $\mathbf{u}^m$, obtained by various means, is available on a part M of the surface of the solid. The two-dimensional M domain can be chosen to include the crack tip or not. The mode I and II SIFs can be computed by least-square methods over the domain M by minimizing the least-square error between the actual field $\mathbf{u}^m$ and an elastic field $\mathbf{u}(\{q\})$ described by a finite set of parameters $\{q\}$, always including the SIFs:

$$\{p\} = \underset{\{q\}}{ArgMin} \int_M \|\mathbf{u}(\{q\}) - \mathbf{u}^m\|^2 dM \tag{27}$$

$$\mathbf{u}(\{q\}) = \sum_{i=1}^{n} q_i U^i(x), \quad n \geqslant 2, \quad U^1 = \mathbf{u}^I, \quad U^2 = \mathbf{u}^{II}, \quad q_1 = K_I, \quad q_2 = K_{II} \tag{28}$$

Different choices can be made for the other fields describing the approximate field $\mathbf{u}(\{p\})$ for $n > 2$: Yoneyama et al. (2007) and Ju et al. (2006) use the solution of the Williams series up to order 10, while Yates et al. (2010), use it up to order 15 by adding, as done by McNeill et al. (1987), a rigid body displacement field to the Williams solution. Hild and Roux (2006), completed this description with linear fields associated with a homogeneous strain field. The optimal set of parameters $\{p\}$ is then solution of the following linear system:

$$[A]\{p\} = \{f\} \quad \text{with} \quad A_{ij} = \int_M U^i \cdot U^j dM, \quad f_i = \int_M U^i \cdot u^m dM \tag{29}$$

Yoneyama et al. (2007), did not fix the position of the crack tip *a priori*, so that the minimization problem was no longer a quadratic one and did not result in a linear system as in (29). Moreover, the crack position parameters appeared in all the expressions of the U^i functions, thus leading to strong coupling between all the parameters. The determination of the crack tip location could also be performed by using hyper-singular fields that correspond to the derivative of the fields with respect to the crack tip position. The equation for the crack tip location was obtained by canceling the contribution of these fields in the fitting of the measured fields *far* from the possible crack tip location (Hamam et al., 2007; Limodin et al., 2010).

Other methods use domain or contour integrals by inserting measured or estimated displacement fields by image correlation into the formula (21), Huntley and Field (1988). This requires computing the stress field. Other authors prefer to use interaction integrals usually employed in post-processing numerical computations (Réthoré et al., 2005, 2008) and as described in Subsection 2.2.

4.2. Estimation of errors on SIFs for plane stress field-based identification

In 3D situations, the solution varies from plane stress at the surface to plane strain in the symmetry plane of the structure for qua-

si-plane problems. Therefore initial insight into the question of the approximation caused by the choice of plane fields for the **u** field can be gained by examining the following problem which provides bounds on the error on the identified SIFs. Let us assume that the real field $\mathbf{u}^m$ corresponds to a plane strain field whose SIFs are denoted by (K_I^m, K_{II}^m),

$$\mathbf{u}^m = K_I^m \mathbf{u}_D^I + K_{II}^m \mathbf{u}_D^{II}, \quad \mathbf{u}_D^i \equiv \mathbf{u}^i(\bar{\nu} = \nu) \quad i = I, II \tag{30}$$

What is the error in the approximate SIFs obtained by the least-squares method with plane stress fields as the fitting target (as usually used in the methods described in the literature)? We shall restrict ourselves to the simplest method where only the singular fields are incorporated in the approximation (28), so that:

$$n = 2, \quad U^i = \mathbf{u}_S^i \equiv \mathbf{u}^i \quad i = I, II \tag{31}$$

If the domain M is a disk centered at the crack tip, then the linear system simplifies it into a diagonal one because of the orthogonality of the mode I and mode II fields for plane stress fields and plane strain fields. The solution is therefore simply:

$$K_i = \frac{\int_M \mathbf{u}_S^i \cdot \mathbf{u}_D^i dM}{\int_M \mathbf{u}_S^i \cdot \mathbf{u}_S^i dM}, \quad i = I, II \tag{32}$$

For M-domains that are disks centered on the crack tip, ratios K_I/K_I^m and K_{II}/K_{II}^m do not depend on the radius of the domain used for identification, and depend only on the Poisson ratio. After several tedious calculations, the error ratios can be obtained in closed-form:

$$E_I(\nu) = \frac{K_I}{K_I^m} - 1 = 2\nu \frac{25 - 136\,\nu + 120\,\nu^2}{157 - 280\,\nu + 125\,\nu^2} \tag{33}$$

$$E_{II}(\nu) = \frac{K_{II}}{K_{II}^m} - 1 = 16\nu^2 \frac{13\,\nu - 19}{245 - 118\,\nu + 149\,\nu^2} \tag{34}$$

The error ratios vanish for a null Poisson ratio, because the plane strain field and plane stress field coincide, while they reach their maximum for incompressible materials. Fig. 4 displays the two error ratios $E_I(\nu)$ and $E_{II}(\nu)$ as a function of the Poisson ratio. It can be seen that the errors behave very differently for the two fracture modes: The mode II error decreases monotonically, whereas the mode I error has a non-monotonic and more extended variation.

By using Irwin's formula, an error on the energy release rate can also be derived from the previous errors on the SIFs. It depends on the Poisson ratio but also on the mix factor η defined as the ratio of the mode-II SIFs over the mode-I SIFs: $\eta = K_{II}^m/K_I^m$:

$$\frac{g}{G}(\nu, \eta) - 1 = \frac{1}{1+\eta^2}\left[\left(\frac{K_I}{K_I^m}\right)^2 + \eta^2\left(\frac{K_{II}}{K_{II}^m}\right)^2\right] - 1 \tag{35}$$

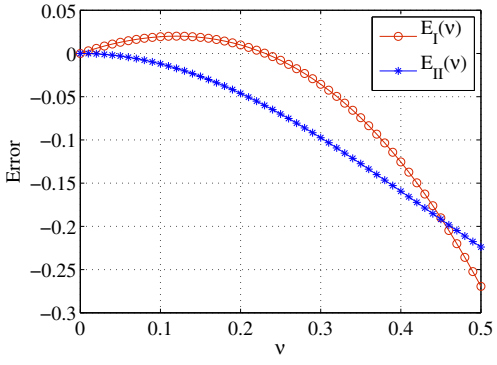

Fig. 4. Error between SIFs computed with plane strain field and that computed with plane stress field, as a function of the Poisson ratio ν.

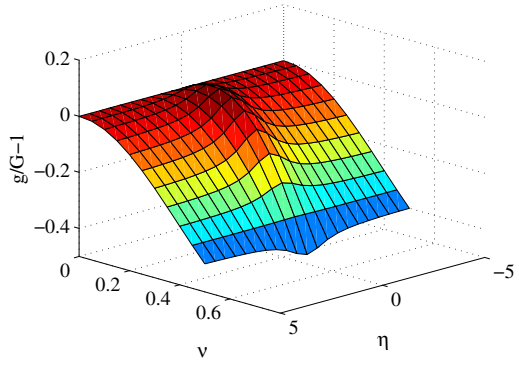

Fig. 5. Error between energy release rate computed with plane strain field and that computed with plane stress field: $(\frac{g}{G}(\nu, \eta) - 1), (0 \leqslant \nu \leqslant 0.5, -5 \leqslant h \leqslant 5)$.

This error function is plotted in Fig. 5. Due to the different behaviors on the errors for Mode I and Mode II, the function has a complex form and generally underestimates the value of G except for a low mix factor and a Poisson ratio close to zero. The maximum error reaches -46% for $\eta = 0$ and $\nu = 0.5$.

5. Computing SIFs and energy release rates from full field surface displacements

Here the aim is to relax the limitations due to the assumption of plane displacement fields for the computation of SIFs and energy release rates from tangential surface measurements in quasi-plane problems, and thus address truly 3D situations. To achieve this we propose computing these quantities from 3D fields that will have been extended into the solid from the surface displacement fields usually measured by DIC on stress free parts of the boundary of the 3D solid.

The method proposed here has two steps. First, a numerical expansion is performed in order to obtain the mechanical fields within the whole solid, from the full-field surface displacement on a part Γ_m, up to the remaining boundary of the solid Γ_u. The problem is formulated as a variant of the well known Cauchy problem for the Lamé operator: provided the tangential displacement field and complete stress traction field are given on Γ_m and are compatible, it is possible to determine the displacement field within the solid. In experiments with full-field measurements, the part where the displacements are measured is generally free of stress and only the tangential displacement can be identified via image correlation with single DIC device. Strictly speaking, the Cauchy data for the Lamé operator has three components of displacement and surface traction fields on Γ_m.

To obtain the displacement field in the solid, it might be preferable to directly compute the elastic solution of the mechanical problem but the true detailed boundary conditions of the solid are almost never known. Only global forces and moments or averaged displacement are available so that additional assumptions are necessary in order to derive a well-posed elastostatic problem. Furthermore, the Cauchy problem can be posed in the region of interest, namely the vicinity of the crack, a far smaller region than the complete solid.

The Cauchy problem is solved by using repeated resolutions of well posed forward problem. The second step is then to compute the quantities of interest (SIFs and/or energy release rates) as described in Section 2.

This procedure requires meshing part of the solid containing the crack, but if the precise location of the crack front is not available then the energy release rates can nevertheless be determined without this information if the G-Theta method is employed. Only the

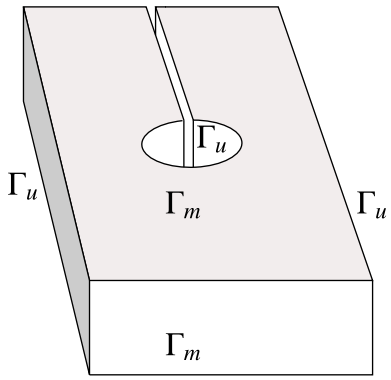

Fig. 6. Domain where the Cauchy problem is posed when the precise location of the crack front is unknown.

crack plane and a cylindrical surface surrounding the crack front must be known beforehand. In this situation, the interior part of the cylinder is not introduced in the model shown in Fig. 6, and the cylindrical surface is obviously a part of the boundary Γ_u.

6. A data completion method for extending surface fields into an elastic solid

The method must now produce a 3D equilibrium elastic displacement field within the solid, provided that the displacement field and the surface traction field are known on part of the boundary, and the distribution of the elastic properties of the material constituting the solid is given. This problem is known as a Cauchy problem for the Lamé operator. The Cauchy problem for elliptic operators has been extensively studied for the Laplace operator used to model the stationary heat equation for homogeneous solids. However, more recently, the Lamé operator has proved interesting for modeling linearized elasticity. The different methods proposed include front propagation methods Bui (1994), moment methods Hon and Wei (2001), fixed point algorithms (Kozlov et al., 1992; Marin and Johansson, 2010b,a), evanescent regularization (Cimetière et al., 2001; Delvare et al., 2010), quasi-reversibility approaches Bourgeois (2005), conformal mapping and Tikhonov regularization (Berntsson and Elden, 2001), boundary element methods by Marin and Lesnic (2002) and direct approaches based on matrix rearrangement Bryan and Caudill (2005). Very few authors have dealt with this 3D problem, either due to the complexity of extending their methods to 3D situations, or computational cost. Nevertheless, using the method of fundamental solutions Marin (2005) dealt with three-dimensional isotropic linear elasticity. In Kadri et al. (2011) the authors identified three-dimensional interface crack via Steklov–Poincaré approach. Whereas, Andrieux and Baranger (2008a, 2012) identified contact area and emerging crack front in 3D framework via energy approaches. Much work has focused on only homogeneous and isotropic media. The present formulation aims at both greater generality in order to deal with more realistic applications, and more computational efficiency in order to deal with large 3D situations. It extends the method given in (Andrieux et al., 2006; Baranger and Andrieux, 2011) for the Cauchy problem for the Laplace operator.

6.1. Statement of the Cauchy problem for the Lamé operator.

An elastic three-dimensional solid Ω is considered, the boundary of which is separated into three non-overlapping parts Fig. 7.

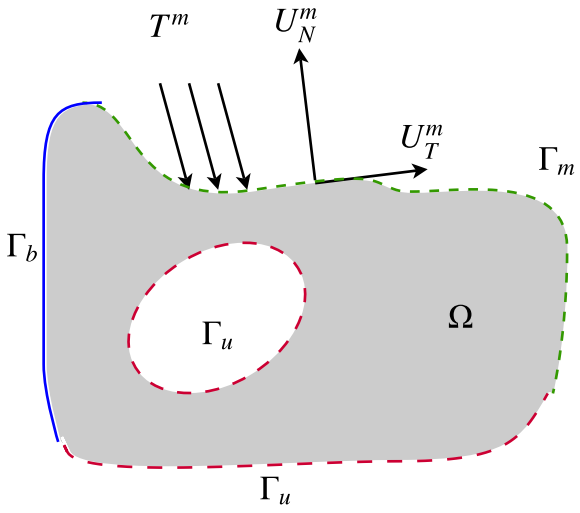

Fig. 7. Definition of the three parts Γ_m, Γ_b and Γ_u of the boundary.

1. On the first part, denoted by Γ_m, the surface traction T^m and the displacement field U^m are known (measured),
2. On the second part, Γ_b, the usual boundary conditions are known (combination of surface traction and displacement field components); these boundary conditions will be denoted generally by:

$$Bu = b \tag{36}$$

3. On the third part, Γ_u, the external forces T^u and the displacement U^u are unknown; both have to be identified.

Provided that the Hooke tensor A of the elastic material forming the solid is known, even if it depends on space, with the usual properties insuring the existence and uniqueness of a classical linear elasticity problem, then the Cauchy problem is the following.

Cauchy problem for the Lamé operator. Given: surface traction field T^m and displacement field U^m on Γ_m, vector b of the usual boundary conditions on Γ_b. Find the surface traction T^u and displacement U^u such that an elastic displacement field $\mathbf{u}$ exists and satisfies the following equilibrium:

$$\begin{cases} div(\mathbf{A} : \varepsilon(\mathbf{u})) = 0 & & in & \Omega \\ \mathbf{A} : \varepsilon(\mathbf{u}) \cdot n = T^m, & \mathbf{u} = U^m & on & \Gamma_m \\ B\mathbf{u} = b & & on & \Gamma_b \\ \mathbf{A} : \varepsilon(\mathbf{u}) \cdot n = T^u, & \mathbf{u} = U^u & on & \Gamma_u \end{cases} \tag{37}$$

The boundary conditions on Γ_m and Γ_u of the solid boundary can be non-linear, as when involving contact and friction. The only requirements for the application of the Cauchy approach for the Lamé operator is that the linear elasticity assumption is satisfied throughout the solid. Existence and uniqueness for the Cauchy problem have been studied extensively for the Laplace operator and more recently for the Lamé operator. Existence is conditioned by a compatibility condition involving the data (U^m, T^m). This condition is an implicit one but it has been shown that the pairs of compatible data are dense in the space $(H^{1/2}(\Gamma_m))^3 \times (H^{-1/2}(\Gamma_m))^3$ of all possible data pairs (Fursikov, 2000). This is the reason why in most applications, the data are assumed to be compatible, especially when originating from possibly noisy measurements: each arbitrarily small neighborhood of the data pair contains a compatible data pair. A notable exception is the work of Cimetière et al. (2001), in which the compatibility condition is explicitly tackled in the discrete problem. If the data is assumed to be compatible, then the Cauchy problem has a unique solution for the Lamé operator with homogeneous and isotropic coefficients (Dehman and

Robbiano, 1993; Ang et al., 1998). The Cauchy Problem formulated here can be seen as an identification problem, namely the identification of unknown boundary conditions on Γ_u, provided overspecified boundary conditions on Γ_m are available: this is therefore an inverse problem, sometimes also known as a data completion problem.

For the applications concerned here, only tangential displacement fields are usually measured on surface Γ_m because single digital camera devices and image correlation techniques are involved. The Cauchy problem is thus slightly modified and takes the following non classical form (Andrieux and Baranger, 2008b).

Incomplete Cauchy problem for the Lamé operator. Given: surface traction field T^m and *tangential* displacement field U^m_t on Γ_m and vector b of usual boundary conditions on Γ_b. Find the surface traction T^u and displacement fields U^u such that an elastic equilibrium displacement field u exists and satisfies.

$$\begin{cases} div(\mathbf{A}:\varepsilon(\mathbf{u}))=0 & in \quad \Omega \\ \mathbf{A}:\varepsilon(\mathbf{u})\cdot n=T^m,\ \mathbf{u}_t=U^m_t & on \quad \Gamma_m \\ B\mathbf{u}=b & on \quad \Gamma_b \\ \mathbf{A}:\varepsilon(\mathbf{u})\cdot n=T^u,\ \mathbf{u}=U^u & on \quad \Gamma_u \end{cases} \tag{38}$$

6.2. Solving the Cauchy problem for the Lamé operator by minimization

In line with (Andrieux and Baranger, 2008a,b), and extending the method of Andrieux et al. (2006), for the Laplacian operator, the general method for solving the Cauchy problem is to derive a functional of the unknown fields on Γ_u, say (τ,υ), where (possibly local) minima provide the desired pair of fields (T^m,U^m) or (T^m,U^m_t). Building this functional requires two steps.

First, the two following elastic displacement fields $\mathbf{u}_1$ and $\mathbf{u}_2$ are defined, as functions of (b,U^m,τ) and (b,T^m,υ) respectively. They correspond to the solutions of two well-posed classical mixed elasticity problems.

$$\begin{cases} div(\mathbf{A}:\varepsilon(\mathbf{u}_1))=0 & in \quad \Omega \\ \mathbf{u}_1=U^m & on \quad \Gamma_m \\ B\mathbf{u}_1=b & on \quad \Gamma_b \\ \mathbf{A}:\varepsilon(\mathbf{u}_1)\cdot n=\tau & on \quad \Gamma_u \end{cases} \qquad \begin{cases} div(\mathbf{A}:\varepsilon(\mathbf{u}_2))=0 & in \quad \Omega \\ \mathbf{A}:\varepsilon(\mathbf{u}_2)\cdot n=T^m & on \quad \Gamma_m \\ B\mathbf{u}_2=b & on \quad \Gamma_b \\ \mathbf{u}_2=\upsilon & on \quad \Gamma_u \end{cases} \tag{39}$$

Since whenever the two fields $\mathbf{u}_1$ and $\mathbf{u}_2$ coincide, then (τ,υ) is a solution (T^u,U^u) of the Cauchy problem, the second step consists in introducing a functional measuring the gap between the two fields. Here, the choice of this functional is the error in the semi-norm of elastic energy:

$$J(\mathbf{u}_1,\mathbf{u}_2)=\frac{1}{2}\int_\Omega \mathbf{A}:\varepsilon(\mathbf{u}_1-\mathbf{u}_2):\varepsilon(\mathbf{u}_1-\mathbf{u}_2)d\Omega \tag{40}$$

The inverse problem is then formulated via the minimization of the energy error functional:

$$\begin{bmatrix} Find\ (\tau,\upsilon)\ that\ minimize\ E(\tau,\upsilon) \\ with\ E(\tau,\upsilon)\equiv J(\mathbf{u}_1,\mathbf{u}_2)=\frac{1}{2}\int_\Omega A:\varepsilon(\mathbf{u}_1-\mathbf{u}_2):\varepsilon(\mathbf{u}_1-\mathbf{u}_2) \\ \mathbf{u}_1=\mathbf{u}_1(b,U^m,\tau),\ \mathbf{u}_2=\mathbf{u}_2(b,T^m,\upsilon)\ solution\ of\ (39) \end{bmatrix} \tag{41}$$

The justification of the formulation lies in the following properties, (Andrieux and Baranger, 2008a):

- E is a positive convex quadratic function,
- If a pair of fields (τ,υ) satisfies $E=0$ then:
  1. $\mathbf{u}_2=\mathbf{u}_1+R$, where R is a solid body displacement field
  2. $\mathbf{u}_1$ solves the Cauchy problem.

For computational purposes, an alternative form of the functional can be derived involving only surface integrals, by exploiting the equilibrium properties of the $\mathbf{u}_i$ fields. The functional$E$ is also given by:

$$\begin{aligned} E(\tau,\upsilon)=&\frac{1}{2}\int_{\Gamma_m}(\mathbf{A}:\varepsilon(\mathbf{u}_1(\tau))\cdot n-T^m)\cdot(U^m-\mathbf{u}_2(\upsilon))d\Gamma \\ &+\frac{1}{2}\int_{\Gamma_u}(\tau-\mathbf{A}:\varepsilon(\mathbf{u}_2(\upsilon))\cdot n)\cdot(\mathbf{u}_1(\tau)-\upsilon)d\Gamma \end{aligned} \tag{42}$$

This last expression is used in the computations and avoids any domain integration. It involves both surfaces Γ_m and Γ_u.

Although the problem is quadratic and could in principle be solved directly via a linear system of equations (the first order optimality condition for J), a direct optimization method should be preferred, using only the gradients of the function. The gradient has to be computed by an adjoint method because of the implicit dependence of the $\mathbf{u}_1$ and $\mathbf{u}_2$ fields with respect to the variables, and the relatively high cost of evaluating the function itself (Chavent, 1991; Griewank, 1993). Going back to the minimization algorithm for the discretized E function, each iteration of the algorithm involves the solution of four linear systems: two direct problems and two adjoint-problems. In order to optimize the computational cost, the Trust Region Method (TRM) is adopted. See Baranger and Andrieux (2008) for details on the numerical aspects of the method.

Once the data completion problem is solved, the elastic displacement field within the entire structure is determined on the finite element mesh that was used for the computation of fields $\mathbf{u}_1$ and $\mathbf{u}_2$. When convergence is reached, $\mathbf{u}_1$ equals $\mathbf{u}_2$, and in the applications field $\mathbf{u}_1$ is used as the "*true*" elastic field in the solid, matching the surface measurements. Afterwards usual numerical methods for computing the SIFs and the energy release rates (Galenne et al., 2005) described above in Section 2 can be employed.

6.3. Noisy Cauchy data and regularization

In real situation, T^m and U^m are measured or approximated, consequently they are noisy and therefore regularisation has to be addressed. Hereafter we denote by $T^{m\delta}$ and $U^{m\delta}$ the noisy Cauchy data, which are known with a noise rate a such as $0<a<1$.

The Cauchy problem solution of the optimization problem (41), is obtained when the functional reaches its minimum. This method has provided promising results in several situation, however as other methods, it becomes unstable in the case of noisy data, and results blow up. During the optimization process, the error reaches a minimum before increasing very fast leading to a numerical explosion, while, the energy functional (42) asymptotically reaches a minimal threshold. This latter is as a function of the noise rate a. In order to overcome this numerical instability, in Rischette et al. (2011) an adequate stopping criteria was developed for the data completion method. This stopping criteria depends on the noise rate and was derived by using a priori errors estimates of the forward problems (39), for more details see Rischette et al. (2011). This criterion is given by:

$$|E_j-E_{j-1}|\leqslant\left(\frac{a}{1-a}\right)^2\left(\|T^{m\delta}\|^2_{\Gamma_m}+\|U^{m\delta}\|^2_{\Gamma_m}\right) \tag{43}$$

where E_j and E_{j-1} are two successive energy function values taken at the iterations j and $j-1$, respectively. Hereafter, only the measured displacement field $U^{m\delta}$ is noisy, the surface traction field $T^m=0$ is known exactly and is free of noise. Hence the above stopping criterion becomes:

$$|E_j-E_{j-1}|\leqslant\left(\frac{a}{1-a}\right)^2\|U^{m\delta}\|^2_{\Gamma_m} \tag{44}$$

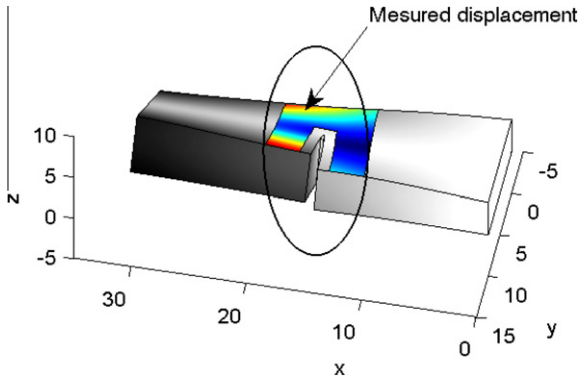

Fig. 8. The solid studied with a crack under mixed Mode-I, II, III loading.

This regularising stopping criteria allows us to avoid instability and then numerical explosion when the noise rate remains reasonable: less than 10%. This regularisation method is used hereafter to control sensitivity to noise.

7. Numerical illustrations

The procedure proposed was tested on numerical data obtained from FE computations. No noise was added to the data but the meshes used for producing the reference solution and computing the fracture mechanics parameter via the solution of the Cauchy problem were different in order to eliminate the inverse problem crime. The difference between the two interpolations of the *data* in the two models nevertheless introduced a form of (small) noise into the problem. It is noteworthy that the measurement surface does not meet the crack intersection with the external surface of the solid. Since displacement discontinuity is likely to occur on the crack surface, usual correlation techniques that rely on regularity assumptions on the displacement fields are not appropriate for dealing with this kind of situation. They must be restricted to parts where the regularity assumptions are valid. Some authors have developed special methods in order to include the possibility of discontinuous displacement across a line (see Section 4), but they usually require knowledge of the position of the crack front, which is sometimes very difficult to achieve, or which necessitates elaborated non linear algorithms when crack position seeking is incorporated.

7.1. 3D loaded cracked specimen

We consider the solid shown in Fig. 8. One of the lateral bases ($x = 0$) of the solid is clamped. On the opposite side ($x = 30$), displacements are prescribed (uniform displacement in the x and y directions, and rotation is prescribed around the x axis which leads to affine prescribed displacement in the y and z directions). The loads applied lead to a mix of Modes I, II, III and the mixity coefficient varies along the crack front. The Cauchy data consist in displacement *measurements* on a well-defined area around the crack, as shown in Fig. 8. The surface traction on this area are equal to zero. The data completion problem is defined only on the part of this solid which is illustrated in Fig. 9. The crack front is considered to be known.

Fig. 9a depicts the data completion domain, with the boundary Γ_m of the Cauchy data and the boundary Γ_u where the displacements and surface traction have to be identified. Fig. 9b shows the associated FE mesh. The isotropic material has the following properties: $E = 2.08\,10^{11}\,Pa$ and $\nu = 0.3$. The identified Stress Intensity Factors and energy release rates are evaluated by using field u_1 obtained after convergence of the minimization problem (41) defined above. Fig. 9b shows the meshed domain. Three cases were studied:

Case 1: we use full displacement data (u_x, u_y and u_z) taken on the patch defined by the area on the face located at $z = 4$.
Case 2: idem Case 1 except that we consider that only tangential displacement components u_x and u_y are known.
Case 3: we use tangential displacement data taken on two identical patches located on the top and bottom sides, at $z = 0$ and $z = 4$, respectively.

The mesh has 12704 nodes whereas the data are given on 259 nodes for each patch.

Fig. 10 show a comparison between reference and identified values. Fig. 10a and b show displacement magnitude on Γ_u and Fig. 10c and d show Mises Stress on Γ_u. Fig. 10h show the displacement and Mises stress, respectively, on the sub-domain around the crack where stress intensity factors and energy release rate are computed. We notice a good agreement with the reference values.

Fig. 11 shows the results obtained in case 1 and Fig. 12 shows the corresponding relative errors. Very good agreement can be seen between the values identified for SIFs and the exact ones (computed from the prescribed loading conditions and a finer mesh, different from that used for solving the Cauchy problem). The variation of Mode II and Mode III SIFs along the crack front (through the thickness of the specimen) is perfectly identified.

Fig. 13 shows the results obtained in cases 2 and 3, Fig. 14 shows the corresponding relative errors. Here, for case 2, a slight degradation of the identification results can be seen for mode I and quite considerable degradation observed for mode III. A physical explanation of this latter degradation is the fact that mode III is

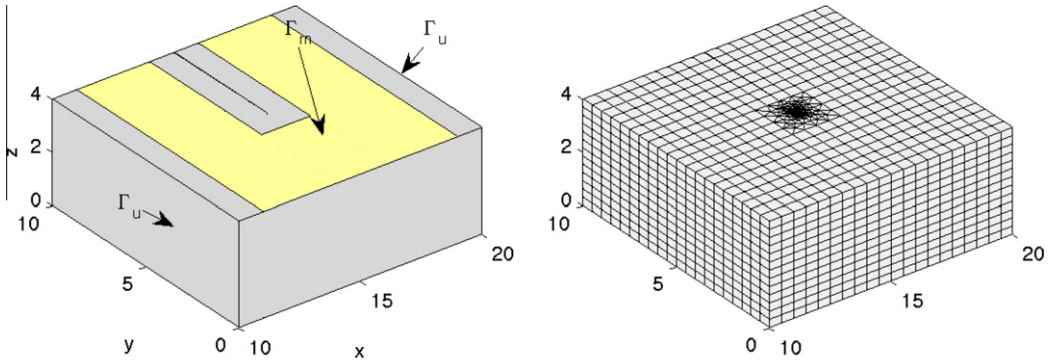

(a) Geometry and boundaries of the data completion domain. (b) Finite element used mesh.

Fig. 9. Geometry and mesh.

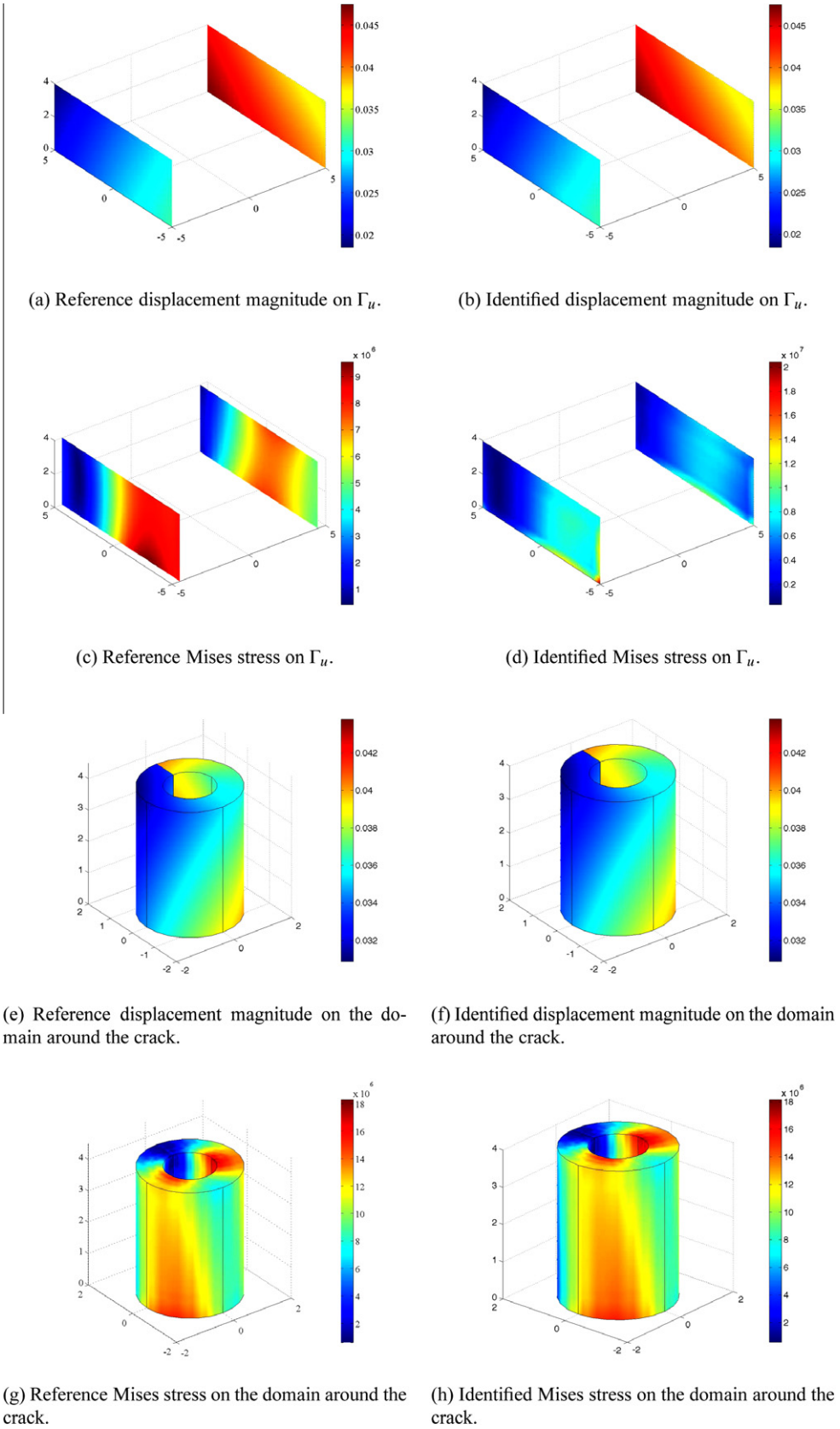

(a) Reference displacement magnitude on Γ_u.

(b) Identified displacement magnitude on Γ_u.

(c) Reference Mises stress on Γ_u.

(d) Identified Mises stress on Γ_u.

(e) Reference displacement magnitude on the domain around the crack.

(f) Identified displacement magnitude on the domain around the crack.

(g) Reference Mises stress on the domain around the crack.

(h) Identified Mises stress on the domain around the crack.

Fig. 10. Reference and identified displacement magnitude (*mm*) and Mises stress (*Pa*) for the case 1.

mainly related to the out-of-plane displacement field. Thus, using only tangential displacements on one side of the specimen leads to poor evaluation of the out-of-plane component of the displacement fields, and thus to imprecise determination of the SIFs of

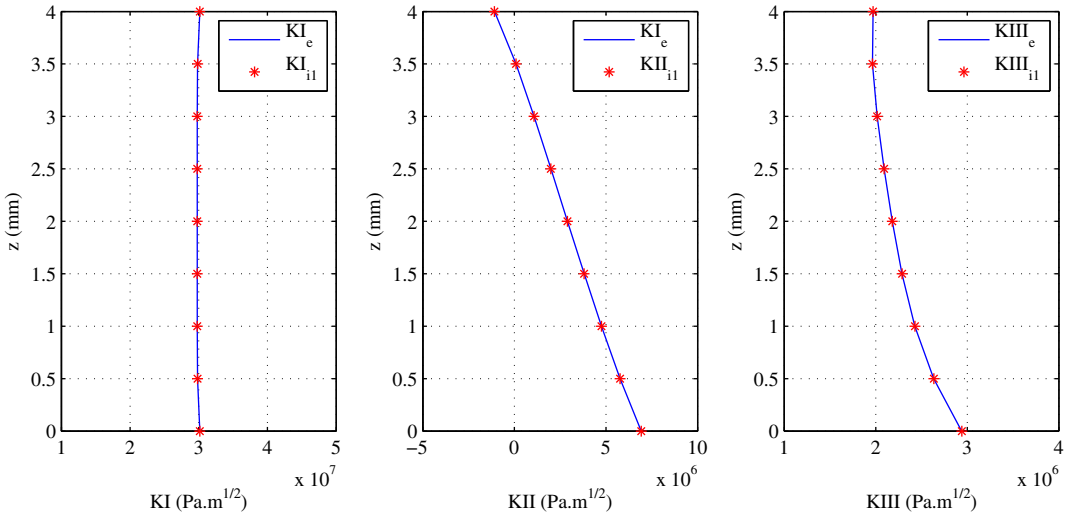

Fig. 11. Identified SIFs KI_i, KII_i and $KIII_i$ $(Pa.m^{1/2})$ along the crack front using full displacement field (u_x, u_y, u_z) on Γ_m. Index e indicates exact (reference) values.

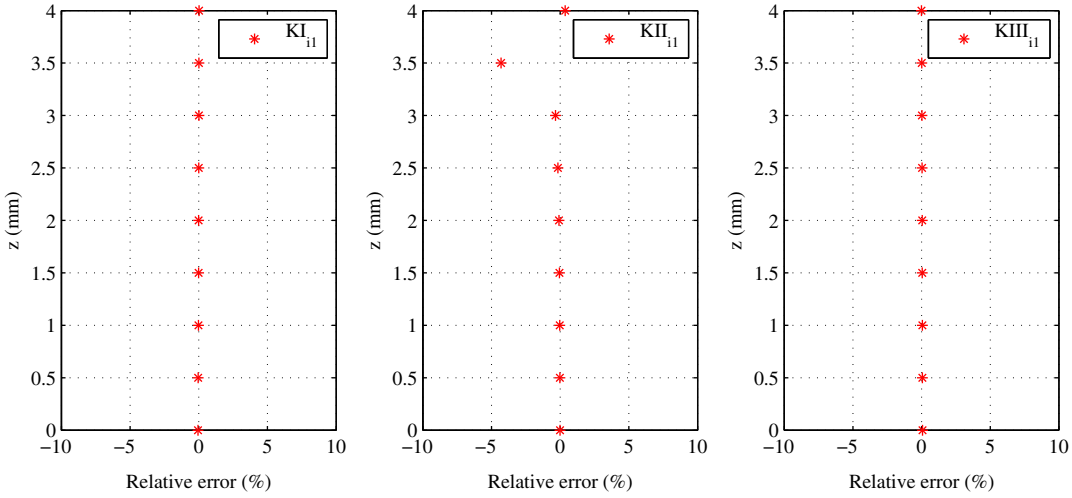

Fig. 12. Relative error of the Identified SIFs KI_i, KII_i and $KIII_i$ $(Pa.m^{1/2})$ along the crack front using full displacement field (u_x, u_y, u_z) on Γ_m. Index e indicates exact (reference) values.

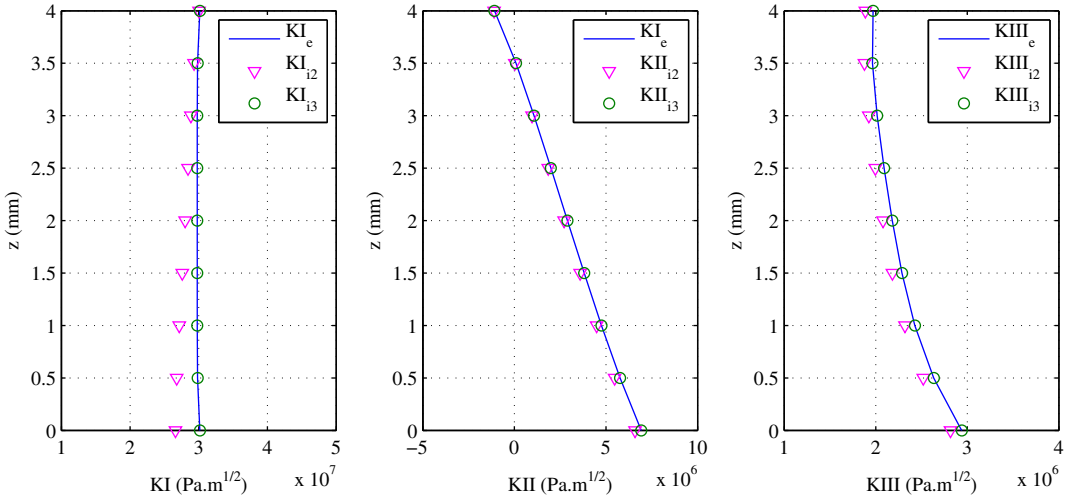

Fig. 13. Identified SIFs KI_i, KII_i and $KIII_i$ $(Pa.m^{1/2})$ along the crack front using tangential displacement field (u_x, u_z) on Γ_m. Indexes 2 and 3 indicate case 2 and case 3, respectively. Index e indicates exact (reference) values.

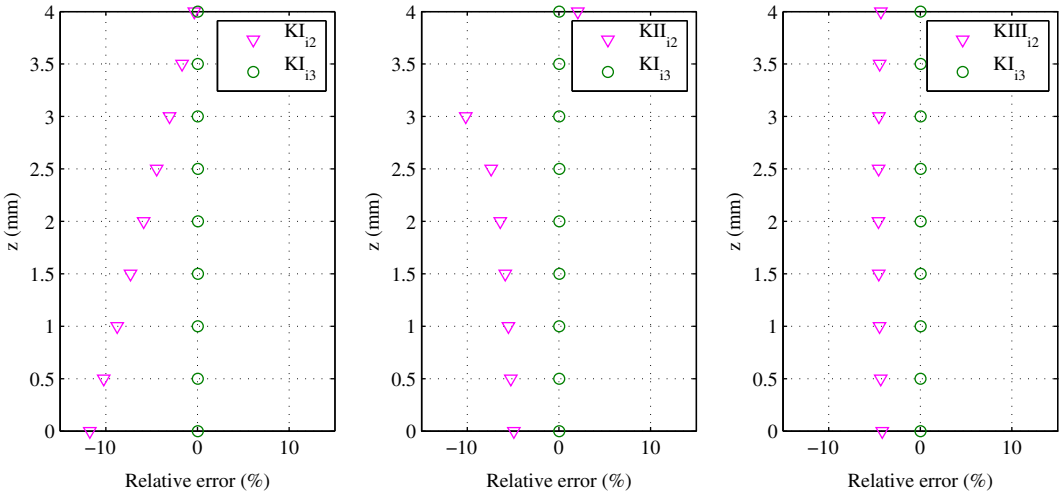

Fig. 14. Relative error of the identified SIFs KI_i, KII_i and $KIII_i$ ($Pa.m^{1/2}$) along the crack front using tangential displacement field (u_x, u_z) on Γ_m. Indexes 2 and 3 indicate case 2 and case 3, respectively. Index e indicates exact (reference) values.

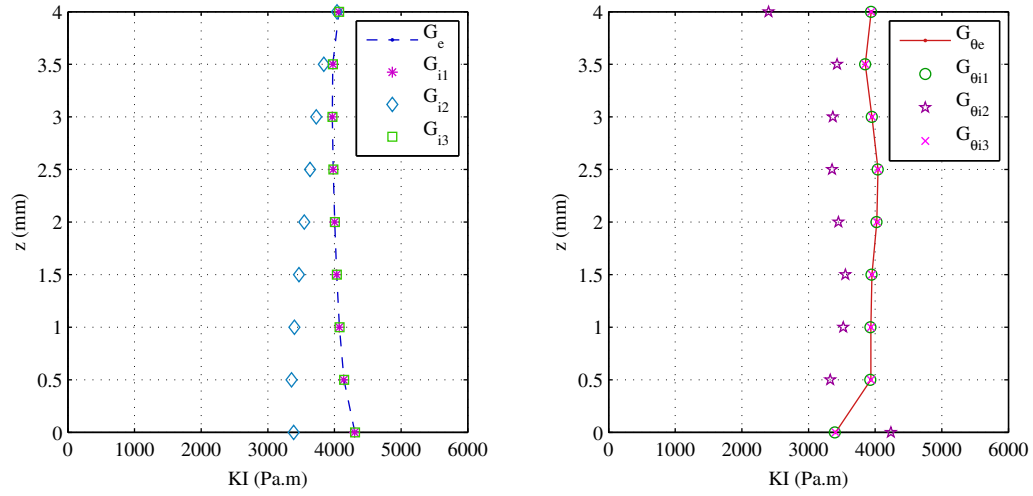

(a) Local energy release rate $g(z)$ computed along the crack front by mean of the Irwin formula and the identified displacement field.

(b) Local energy release rate $g(z)$ computed along the crack front by mean of the G-Theta method and the identified displacement field.

Fig. 15. Comparison of the exact and identified $g(z)$ ($Pa.m$): index e denotes exact value, index i indicates identified one and indexes 1, 2 and 3 indicate case 1, 2 and 3, respectively.

mode III. Furthermore, these results required far more iterations in the minimization process used to solve the data completion step of the procedure than those of case 1. This was due to the same reason: controlling the out-of-plane displacement field is much more difficult.

When increasing the amount of data, and if the information is arranged geometrically by using both faces of the mock-up (case 3), then even with only tangential data, good agreement can be obtained again between the exact and identified values for the same computational cost. The SIFs are computed here by the least-square fitting method on the discontinuities of the displacement across the crack (20) over a segment of length 1.5. A global view on the results is given by the examination of the elastic energy release rate along the crack front, obtained from the SIFs by using the Irwin formula. Fig. 15a shows the local energy release rate identified as a function of the space variable through the thickness $g(z)$ obtained in the three cases defined above and compared to the exact one. Fig. 16a and b show, respectively, the relative error of the local energy release rate computed by Irwin formula and G-Theta method.

Again, the results for case 2, where tangential displacements on only one side of the specimen are available, are far less accurate than the results obtained in the other cases. The global energy release values (that is the integration over the thickness of $g(z)$) are summarized in Table 1.

The local energy release rates $g(z)$ can also be computed directly by the G-Theta method, thereby avoiding the computation of the SIFs. This method can be used when the precise location of the crack front is unknown, see Section 5. Fig. 15b gathers the local elastic release rate curves for the three cases studied. The functions are computed with an interpolation by Legendre polynomials up to order 7 (see Galenne et al., 2005).

The results for cases 1 and 3 are very accurate, and for reasons already given, case 2 is quite far from the reference values. The

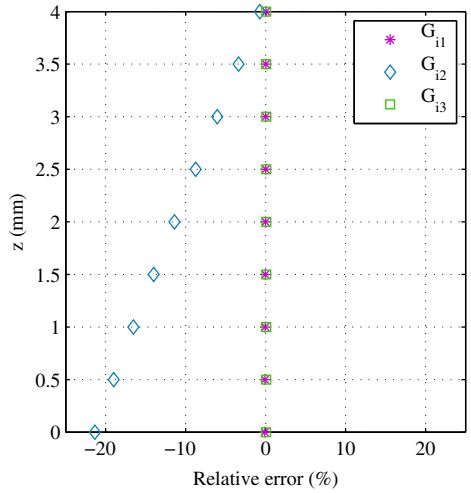

(a) Relative error of the local energy release rate $g(z)$ computed along the crack front by mean of the Irwin formula and the identified displacement field.

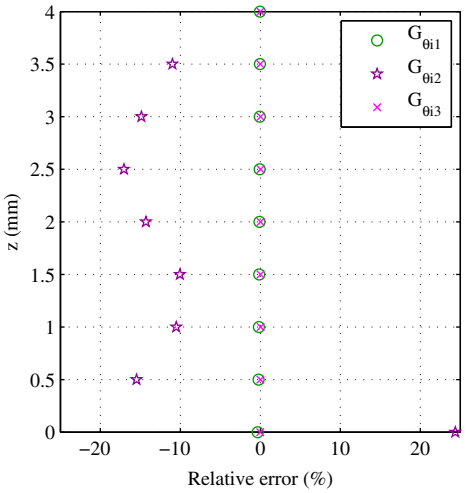

(b) Relative error of the local energy release rate $g(z)$ computed along the crack front by mean of the G-Theta method and the identified displacement field.

Fig. 16. Comparison of the exact and identified $g(z)$ $(Pa.m)$: index i indicates identified one and indexes 1, 2 and 3 indicate case 1, 2 and 3, respectively.

Table 1
Global energy release rates. Comparison between the three cases and the exact computation: $G_e = 16093\,Pa.m$.

Global $G\,(Pa.m)$	Case 1	Case 2	Case 3
Identified	16153	14342	16105
Relative error	−0.37%	12.2%	−0.074%

results are very similar to those obtained with SIFs computations and the Irwin formula and no clear conclusion can be given with respect to the respective merits of the two methods.

7.2. Bi-material CT specimen

The next application is devoted to a Compact Tension specimen (CT), constituted with two distinct elastic materials, and for which the crack is slightly shifted from the geometrical symmetry plane, as shown in Fig. 17a. The tangential displacements are detected by patches arranged on the upper surface and on one of the side surfaces of the specimen, as depicted in Fig. 17b.

The specimen is loaded by prescribing divergent horizontal displacements on lines A and B. It has a thickness of 20 mm. The materials have Poisson ratios of $\nu_1 = 0.2$ $\nu_2 = 0.4$, respectively, and the ratio of the Young moduli is five. The crack is located in the less stiff material (material 2).

The Cauchy problem is solved on a sub-domain surrounding the crack tip line, as shown on Fig. 18a and b. Γ_m is the part where tangential displacement is given together with zero surface traction (the patches); Γ_u is the part where the displacement and surface traction are reconstructed, while the other faces are free of surface traction. The Γ_m part contains 481 nodes, and the Γ_u one contains 341 nodes. The data completion problem is solved with 12 global

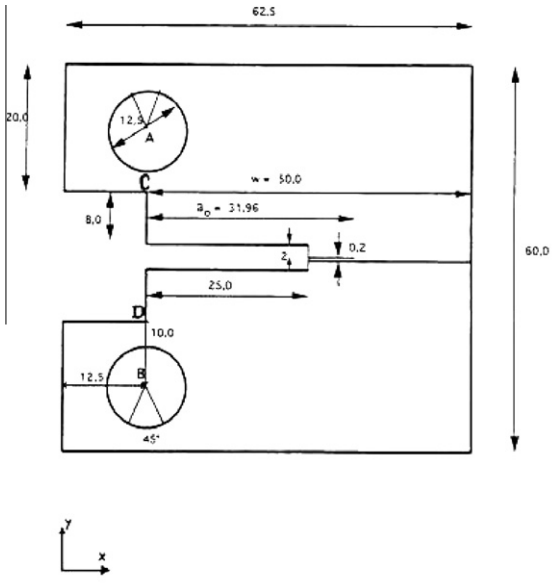

(a) Geometry of the bi-material CT specimen (mm).

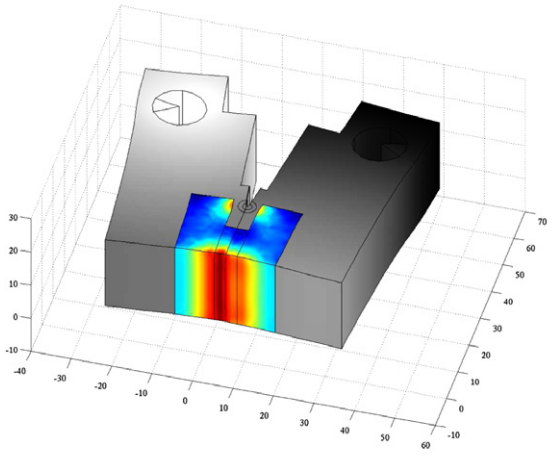

(b) Location of the two patches where the tangential displacement field is known.

Fig. 17. Geometry and Cauchy data.

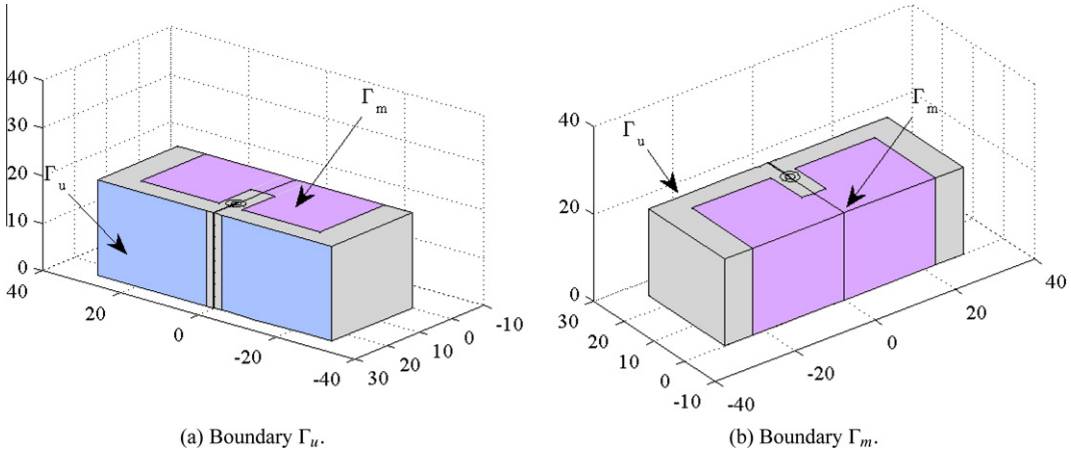

Fig. 18. Geometry of the sub-domain where the Cauchy problem is solved.

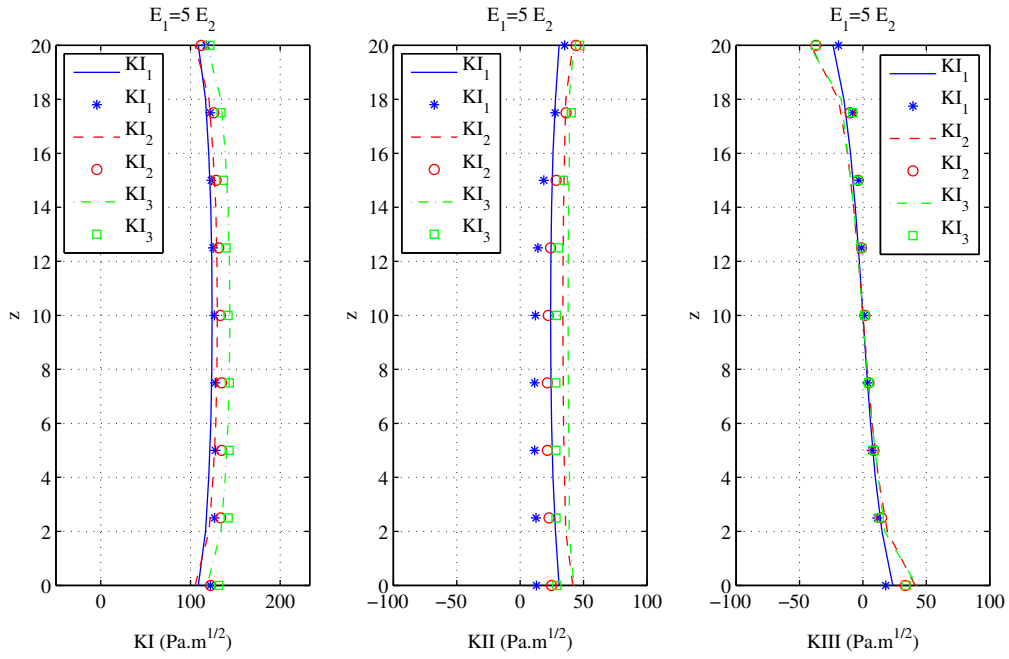

Fig. 19. Comparison of identified SIFs (mark) with reference SIFs (line) through the thickness of the specimen for each fitting procedure. 1 term in the fitting procedure: — Reference, ∗ Identified; 2 term in the fitting procedure: -- Reference, ○ Identified; 3 term in the fitting procedure: ··· Reference, □ Identified.

iterations of the process described in 6.2, which requires the resolution of 48 3D-elastic problems (four solutions per iteration: two direct problems and two adjoint problems) with the same stiffness matrix. In this case, the vicinity of the interface to the crack, leads to a form of the displacement jump across the crack that is significantly different from its classical asymptotic form (variation as $r^{1/2}$), even very close to the crack tip. The computation of the SIFs must take this specific feature into account as poor evaluation of the SIFs would result in fitting the actual jump with only the singular part of the theoretical displacement field. To deal with this issue, we add the second and third terms of the Williams' series in the fitting procedure which then read as (for one component of the displacement jump denoted by $[u]$):

$$\begin{cases} (K,A,B) = \underset{k,\alpha,\beta}{ArgMin} \int_0^{r_m} \left([u] - k\sqrt{r} - \alpha r - \beta r\sqrt{r}\right)^2 dr \\ [u] = K\sqrt{r} + Ar + Br\sqrt{r} \end{cases} \tag{45}$$

Table 2
Global energy release rates.

Global $G(Pa.m)$	Fitting method with one term	Fitting method with two terms	Fitting method with three terms
Reference	6.431	7.227	8.827
Identified	6.741	7.563	8.641
Relative error	−4.82%	−4.64%	2.1%

where r_m is the length of the segment where the displacements are fitted. This problem has a closed form solution for the expression of the identified stress intensity factor, which is the $\sqrt{r}$ component K of the displacement jump:

$$K^{(3)} = \frac{450}{r_m^2}\int_0^{r_m}[u]\sqrt{r}dr - \frac{1260}{r_m^{5/2}}\int_0^{r_m}[u]rdr + \frac{840}{r_m^3}\int_0^{r_m}[u]r\sqrt{r}dr \tag{46}$$

A similar expression can be obtained when using only the two first terms of the Williams series.

$$K^{(2)} = \frac{50}{r_m^2}\int_0^{r_m}[u]\sqrt{r}dr - \frac{60}{r_m^{5/2}}\int_0^{r_m}[u]rdr \tag{47}$$

Obviously, the values of the computed SIFs are different and will be denoted by an index 1, 2 or 3 depending on the number of terms of the series used in the fitting procedure.

It can first be seen that for Mode I and Mode II the corrections brought about by the addition of new terms of the Williams series in the fitting procedure are significant and that it can be considered that *convergence* is obtained with three terms in the series. Next, Fig. 19 shows that very good precision is obtained in the reconstruction of the SIFs through the thickness. Table 2 gathers the results for the global release rate G (which is a virtual propagation celerity uniformly distributed through the thickness). The same remarks apply as for the SIFs.

The global energy release rate value can be compared with the value G_{PS} obtained by directly exploiting the surface displacement fields with the plane stress assumption, which is the usual method when using full field measurements on a quasi-plane specimen (see Subsection 4.1). The computed value of $G_{PS} = 7.62\,Pa.m$ then exhibits an error (underestimation) up to 13.7%. This result can be explained first by the error of the "*plane part*" on the global release rate (related to the two first SIFs in the Irwin formula (11), and secondly with a smaller influence, by the existence of a non vanishing SIF of the Mode III. Both effects are clearly seen to lead to an underestimation of the global release rate G. Another effect that leads to a supplementary error, but is hardly considered as an over or underestimation, is the fact that the singularity of the surface field for 3D situation is known to be different from the classical $r^{1/2}$ one (see Sections 1 and 3). These three sources of error indicate that strong three-dimensional effects are encountered in this quasi-plane situation.

As mentioned previously, when the precise location of the crack front is not known, the energy release rate can nevertheless be evaluated by a similar method but with an adapted domain for the extension of the displacement field into the solid, excluding a zone around the crack front, as depicted in Fig. 20.

For the case with the same material constants in materials 1 and 2, for example, the identified global energy release rate is $G_i = 21.84\,Pa.m$ for a reference value of $G_r = 22.29\,Pa.m$, thus leading to a −2% error. The estimation by the plane stress Rice integral computed for surface displacement only is $G_{PS} = 23.64\,Pa.m$, that is to say an error of 6.1%.

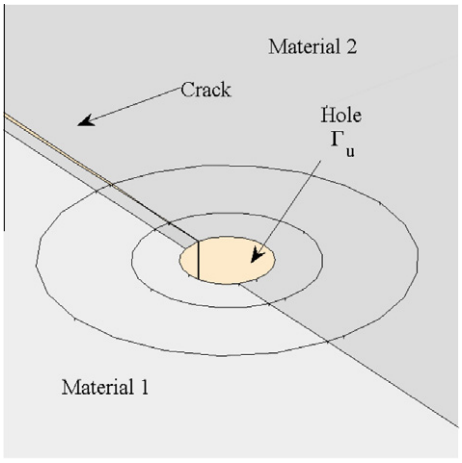

Fig. 20. Zoom on the domain used for the data completion problem when the crack front is unknown.

8. Conclusion

In this paper we addressed the question of determining the quantities of 3D linear fracture mechanics in a structure by using surface displacement field measurements. The method relies on the extension of these fields inside the (elastic) solid. This approach makes it possible to deal with truly three-dimensional situations (geometry and loading) and overcome the imprecision encountered with quasi-plane situations, where boundary layer effects can disqualify the simple analysis of surface fields by usual methods based on the plane stress assumption. A short study of these phenomena and on the estimation of errors made with this kind of analysis was performed. The precision of the results are quite satisfactory but it should be recalled that they are obtained by comparison with synthetic data where no noise is added, apart the interpolation noise. Numerical experiments reported elsewhere (Andrieux et al., 2006; Andrieux and Baranger, 2008a; Andrieux and Baranger, 2008b; Baranger and Andrieux, 2011; Andrieux and Baranger, 2012; Kadri et al., 2011) have nevertheless shown that with the precision currently obtained in DIC devices and DIC techniques (rate noise less than 5%), there is no need for any regularisation except an *ad hoc* stopping criterion. It should be noted that in this paper, only tangential displacements on a part of the external boundary are used because this situation is encountered when the measurements involve only one DIC. With stereoscopic devices involving two cameras, the full displacement field is available, and the same approach can be used without modifications. This situation is more favorable for the first step of the method (data completion problem) because of the increase in the quality and amount of data. Forthcoming work will include experiments with DIC measured data and an additional regularisation procedure acting on the identified data of the Cauchy problem.

References

Andrieux, S., Baranger, T., Ben Abda, A., 2006. Solving Cauchy problems by minimizing an energy-like functional. Inverse Probl. 22, 115–133.
Andrieux, S., Baranger, T.N., 2008a. An energy error-based method for the resolution of the Cauchy problem in 3d linear elasticity. Comput. Methods Appl. Mech. Engrg. 197, 902–920.
Andrieux, S., Baranger, T.N., 2008b. Energy methods for Cauchy problems of evolutions equations. J. Phys: Conf. Ser. 135, 012007.
Andrieux, S., Baranger, T.N., 2012. Emerging crack front identification from tangential surface displacements. C. R. Mec. 340, 565–574.
Ang, D.D., Ikehata, M., Trong, D.D., Yamamoto, M., 1998. Unique continuation for a stationary isotropic lamé system with variable coefficients. Comm. Partial Differential Equations 23, 599–617.
Baranger, T., Andrieux, S., 2011. Constitutive law gap functionals for solving the Cauchy problem for linear elliptic pde. Appl. Math. Comput. 218, 1970–1989.
Baranger, T.N., Andrieux, S., 2008. An optimization approach for the Cauchy problem in linear elasticity. Struct. Multidiscip. Optim. 35, 141–152.
Berntsson, F., Elden, L., 2001. Numerical solution of a Cauchy problem for the laplace equation. Inverse Probl. 17, 839.
Bourgeois, L., 2005. A mixed formulation of quasi-reversibility to solve the Cauchy problem for laplace's equation. Inverse Probl. 21, 1087–1104.
Bryan, K., Caudill, L., 2005. Reconstruction of an unknown boundary portion from Cauchy data in n dimensions. Inverse Probl. 21, 239.
Bui, H.D., 1978. Mécanique de la Rupture Fragile. Masson.
Bui, H.D., 1983. Associated path independent j-integrals for separating mixed modes. J. Mech. Phys. Solids 31, 439–448.
Bui, H.D., 1994. Inverse Problems in the Mechanics of Materials: an Introduction. CRC Press, Boca Raton.
Bui, H.D., 2006. Fracture Mechanics: Inverse Problems and Solutions. Springer.
Chavent, G., 1991. On the theory and practice of non-linear least-squares. Adv. Water Res. 14, 55–63.
Cimetière, A., Delvare, F., Jaoua, M., Pons, F., 2001. Solution of the Cauchy problem using iterated Tikhonov regularization. Inverse Probl. 17, 553–570.
Dehman, B., Robbiano, A., 1993. La propriété du prolongement unique pour un système elliptique: le système de lamé. J. Math. Pure. Appl. 72, 475–492.
Delvare, F., Cimetiére, A., Hanus, J.L., Bailly, P., 2010. An iterative method for the Cauchy problem in linear elasticity with fading regularization effect. Comput. Methods Appl. Mech. Engrg. 199, 3336–3344.
Destuynder, P., Jaoua, M., 1981. Sur une interprétation de l'intégrale de rice en théorie de la rupture fragile. Math. Methods Appl. Sci. 3, 70–87.

Destuynder, P., Jaoua, M., Lescure, S., 1983. Quelques remarques sur la mécanique de la rupture élastique. J. Mec. Theor. Appl. 2, 113–135.
Fursikov, A.V., 2000. Optimal Control of Distributed Systems. American mathematical Society.
Galenne, E., Boiteau, O., Visse, E., 2005. Taux de restitution d'énergie en thermo-élasticité linéaire. Code-Aster Documentation numberR7-02-01. EDF E&D.
Griewank, A., 1993. Some bounds on the complexity og gradients, jacobians and hessians. Technical Report numberMCS-P355-0393. Mathematics and Computer Science Division, Argonne National Laboratory.
Hamam, R., Hild, F., Roux, S., 2007. Stress intensity factor gauging by digital image correlation: application in cyclic fatigue. Strain 43, 181–192.
Hild, F., Roux, S., 2006. Measuring stress intensity factors with a camera: integrated digital image correlation (i-dic). C. R. Mec. 334, 8–12.
Hon, Y.C., Wei, T., 2001. Backus–Gilbert algorithm for the Cauchy problem of the laplace equation. Inverse Probl. 17, 261.
Huntley, J., Field, J., 1988. Measurement of crack tip displacement field using laser speckle photography. Eng. Fract. Mech. 30, 779–790.
Irwin, G.R., 1957. Analysis of stresses and strains near the end of a crack traversing a plate. J. Appl. Mech. 17, 261–271.
Ju, S., Liu, S., Liu, K., 2006. Measurement of stress intensity factors by digital camera. Internat. J. Solids Structures 43, 1009–1022.
Kadri, M.L., Abdallah, J.B., Baranger, T.N., 2011. Identification of internal cracks in a three-dimensional solid body via Steklov–Poincaré approaches. C. R. Mec. 339, 674–681.
Kozlov, V.A., Maz'ya, V.G., Fomin, A.F., 1992. An iterative method for solving the Cauchy problem for elliptic equations. Comput. Math. Phys. 31, 45–52.
Leblond, J., 2003. Mécanique de la Rupture Fragile et Ductile. Hermes Science Publications.
Li, F., Shih, C., Needleman, A., 1985. A comparison of methods for calculating energy release rates. Eng. Fract. Mech. 21, 405–421.
Li, Z., Guo, W., Kuang, Z., 2000. Three-dimensional elastic stress fields near notches in finite thickness plates. Internat. J. Solids Structures 37, 7617–7632.
Limodin, N., Réthoré, J., Buffire, J.Y., Hild, F., Roux, S., Ludwig, W., Rannou, J., Gravouil, A., 2010. Influence of closure on the 3d propagation of fatigue cracks in a nodular cast iron investigated by *X*-ray tomography and 3d volume correlation. Acta Mater. 58, 2957–2967.
Marin, L., 2005. A meshless method for solving the Cauchy problem in three-dimensional elastostatics. Comput. Math. Appl. 50, 73–92.
Marin, L., Johansson, B.T., 2010a. A relaxation method of an alternating iterative algorithm for the Cauchy problem in linear isotropic elasticity. Comput. Methods Appl. Mech. Engrg. 199, 3179–3196.
Marin, L., Johansson, B.T., 2010b. Relaxation procedures for an iterative MFS algorithm for the stable reconstruction of elastic fields from Cauchy data in two-dimensional isotropic linear elasticity. Internat. J. Solids Structures 47, 3462–3479.
Marin, L., Lesnic, D., 2002. Regularized boundary element solution for an inverse boundary value problem in linear elasticity. Comm. Numer. Methods Engrg. 18, 817–825.
McNeill, S., Peters, W., Sutton, M., 1983. A study of fracture mechanics parameters by digital image processing, In 18th Midwestern Mechanic Conference, pp. 267–271.
McNeill, S., Peters, W., Sutton, M., 1987. Estimation of stress intensity factor by digital image correlation. Eng. Fract. Mech. 28, 101–112.
Noda, N.A., Kagita, M., 2004. Variations of stress intensity factors of a semi-elliptical surface crack subjected to mode i, ii, iii loading. Int. J. Press. Vessels Pip. 81, 635–644.
Parsons, I., Hall, J., 1989. A finite element investigation of the elastostatic state near a three dimensional edge crack. Eng. Fract. Mech. 33, 45–63.
Réthoré, J., Gravouil, A., Morestin, F., Combescure, A., 2005. Estimation of mixed-mode stress intensity factors using digital image correlation and an interaction integral. Int. J. Fract. 132, 65–79.
Réthoré, J., Roux, S., Hild, F., 2008. Noise-robust stress intensity factor determination from kinematic field measurements. Eng. Fract. Mech. 75, 3763–3781.
Rice, J.R., 1968. A path independent integral and the approximate analysis of strain concentration by notches and cracks. J. Appl. Mech. 35, 379–386.
Rischette, R., Baranger, T.N., Debit, N., 2011. Numerical analysis of an energy-like minimization method to solve Cauchy problem with noisy data. J. Comput. Appl. Math. 235, 3257–3269.
Rosakis, A.J., Ravi-Chandar, K., 1986. On crack-tip stress state: an experimental evaluation of three-dimensional effects. Internat. J. Solids Structures 22, 121–134.
Sinha, J.K., Tippur, H.V., Xu, L., 1997. An interferometric and finite element investigation of interfacial crack tip fields: role of mode-mixity on 3-d stress variations. Internat. J. Solids Structures 34, 741–754.
Williams, M.L., 1957. On the stress distribution at the base of a stationary crack. J. Appl. Mech. 24, 109–114.
Yates, J.R., Zanganeh, M., Tai, Y.H., 2010. Quantifying crack tip displacement fields with dic. Eng. Fract. Mech. 77, 2063–2076. International Conference on Crack Paths 2009.
Yoneyama, S., Ogawa, T., Kobayashi, Y., 2007. Evaluating mixed-mode stress intensity factors from full-field displacement fields obtained by optical methods. Eng. Fract. Mech. 74, 1399–1412.
Zhang, B., Guo, W., 2007. Three-dimensional stress state around quarter-elliptical corner cracks in elastic plates subjected to uniform tension loading. Eng. Fract. Mech. 74, 386–398.